Phonon dispersion and polar-optical scattering in 2*H* PbI_2

Yia-Chung Chang
Department of Physics and Materials Research Laboratory, University of Illinois at Urbana-Champaign, 1110 West Green Street, Urbana, Illinois 61801

R. B. James
Advanced Electronics Manufacturing Technologies Department, Sandia National Laboratories, Livermore, California 94551
(Received 10 September 1996)

Theoretical studies of phonon-dispersion curves and the polar-optical scattering process for 2*H* PbI_2 are presented. A rigid-ion model with anisotropic effective charges is used to calculate the phonon-dispersion curves. The carrier mobility and its anisotropy due to polar-optical scattering as a function of temperature are calculated. Results are in good agreement with the experimental data. [S0163-1829(97)02013-4]

I. INTRODUCTION

PbI_2 is one of the candidate materials for room-temperature x-ray and γ-ray radiation detectors.[1] The electronic structures and optical properties were studied both experimentally[2–6] and theoretically.[7–9] It was determined that PbI_2 is direct with both the conduction-band minimum and valence-band maximum occurring at the *A* point. The conduction band states are derived from the spin-orbit split 6*p* orbitals of Pb, while the valence-band states are derived from the 6*s* orbitals of Pb and $5p_z$ orbitals of I. The phonon properties have been studied via neutron scattering,[10] reflectivity,[11,12] and Raman[13] measurements. The carrier mobilities were determined by Hall measurements[14] and *I-V* studies.[15] Up to now, theoretical calculations of the phonon modes and carrier transport properties have not been reported. The carrier transport is an important consideration for applications in room-temperature radiation detectors. In this paper, we present theoretical studies of both the phonon and transport properties of PbI_2 via the use of a rigid-ion model and polar-optical scattering. Based on our previous studies of HgI_2,[16] the polar-optical scattering is the dominant mechanism responsible for intrinsic carrier transport. Since PbI_2 is similar to HgI_2, we expect the same holds true. Our calculated electron mobilites based on polar-optical scattering alone are in fairly good agreement with experiment (within a factor of 3), indicating that the currently observed electron mobilities are probably limited by the intrinsic scattering mechanism.

In Sec. II, we present the rigid-ion model calculation for the phonon-dispersion curves of 2*H* PbI_2. In Sec. III, we describe the polar-optical scattering for noncubic crystals and examine the angular dependence of the electron-phonon coupling constant for PbI_2. In Sec. IV, we discuss our calculated results for carrier scattering rates and mobilities as functions of temperature. A summary of the paper is given in Sec. V.

II. PHONON-DISPERSION CURVES

To calculate the phonon-dispersion curves in the rigid-ion model, we need to fully utilize the symmetry properties of the crystal. The 2*H* PbI_2 has a hexagonal lattice with the unit cell depicted in Fig. 1. Pb (I) atoms are labeled by 1 (2 or 3) with or without superscript. The lattice constants used are $a=4.56$ Å and $c=6.98$ Å. The primitive lattice vectors are $\mathbf{a}_1=(\sqrt{3}/2,-1/2,0)a$, $\mathbf{a}_2=(0,1,0)a$, and $\mathbf{a}_3=(0,0,1)c$ in Cartesian coordinates. The Pb atom in the unit cell is placed at the origin, and the two I atoms are placed at $\mathbf{u}_1=\frac{2}{3}\mathbf{a}_1+\frac{1}{3}\mathbf{a}_2+0.265\mathbf{a}_3$ and $\frac{1}{3}\mathbf{u}_2=\mathbf{a}_1+\frac{2}{3}\mathbf{a}_2+0.265\mathbf{a}_3$. The reciprocal-lattice vectors are

$$\mathbf{b}_1=(2/\sqrt{3},0,0)(2\pi/a),$$

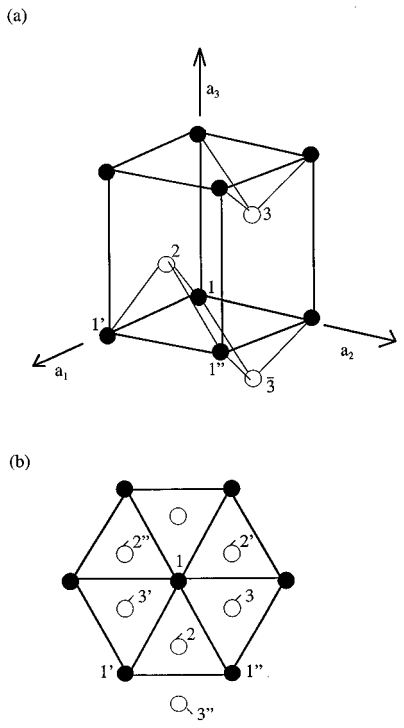

FIG. 1. (a) Crystal structure of PbI_2 with Pb atom labeled by 1 and I atoms labeled by 2 and 3. (b) Projection of the crystal onto the *xy* plane. The nearest-neighbor I atoms centered at Pb atom 1 are labeled by 2, 2′, and 2″ in counterclockwise order. Similarly, the nearest-neighbor I atoms centered at I atom 2 are labeled by 3, 3′, and 3.″

TABLE I. The matrix representation of symmetry operations of the point group for PbI_2.

$$E=\begin{pmatrix}1&0&0\\0&1&0\\0&0&1\end{pmatrix} \qquad \sigma_d=\begin{pmatrix}1&0&0\\0&-1&0\\0&0&1\end{pmatrix}$$

$$C_3=\begin{pmatrix}-\frac{1}{2}&\frac{\sqrt{3}}{2}&0\\-\frac{\sqrt{3}}{2}&-\frac{1}{2}&0\\0&0&1\end{pmatrix} \qquad C_3^{-1}=\begin{pmatrix}-\frac{1}{2}&-\frac{\sqrt{3}}{2}&0\\\frac{\sqrt{3}}{2}&-\frac{1}{2}&0\\0&0&1\end{pmatrix}$$

$$C_3\sigma_d=\begin{pmatrix}-\frac{1}{2}&-\frac{\sqrt{3}}{2}&0\\\frac{\sqrt{3}}{2}&\frac{1}{2}&0\\0&0&1\end{pmatrix} \qquad C_3^{-1}\sigma_d=\begin{pmatrix}-\frac{1}{2}&\frac{\sqrt{3}}{2}&0\\-\frac{\sqrt{3}}{2}&\frac{1}{2}&0\\0&0&1\end{pmatrix}$$

$$\mathbf{b}_2=(1/\sqrt{3},1,0)(2\pi/a),$$

and

$$\mathbf{b}_3=(0,0,1)(2\pi/c).$$

The first Brillouin zone is shown in Fig. 3 of Ref. 8.

The point group of the crystal is D_{3d} with 12 elements. Six symmetry operations are denoted by E, C_3, C_3^{-1}, $\sigma_d, \sigma_d C_3, \sigma_d C_3^{-1}$, where E is the identity, C_3 is a threefold rotation about the c axis, and σ_d an x-z mirror plane. The matrix representation of the six operations are given in Table I. The remaining six symmetry operations are products of the above with the inversion (denoted by I). The irreducible representations of the D_{3d} point group are denoted by A_{1g}, A_{2u}, B_g, E_g, and E_u. The A B representations are one dimensional and the E representations are two dimensional. The subscripts g and u denote symmetries which are even (*gerade*) and odd (*ungerade*) under inversion.

Since there are three atoms per unit cell, we expect to find nine phonon branches. The polarization vectors of zone-center phonons should transform according to the irreducible representations of the group D_{3d}. Due to the existence of an inversion center which falls on a Pb atom, the symmetry identification of the zone-center phonon modes is quite easy. First we classify the symmetry of phonon modes by its parity. A displacement of the Pb atom alone is denoted by a vector $\mathbf{d}_1$, which has an odd parity, since the vector will flip sign under inversion. A simultaneous displacement of two I atoms in the unit cell in the same direction (denoted by $\mathbf{d}_+=\mathbf{d}_2+\mathbf{d}_3$) also has an odd parity, while a simultaneous displacement of two I atoms in opposite directions (denoted by $\mathbf{d}_-=\mathbf{d}_2-\mathbf{d}_3$) has an even parity. Thus, odd-parity modes must have a polarization vector which is a linear combination of $\mathbf{d}_1$ and $\mathbf{d}_+$, and even-parity modes must behave like $\mathbf{d}_-$. Taking into account the three possible directions (x,y,z) we end up with six odd-parity modes (three acoustical and three optical) and three even-parity optical modes. The three z vibrations transform according to the A representation, and the x,y vibrations transform according to the twofold E representation. Therefore, the three acoustical modes can be identified as the $A_{2u}(LA)$ and $E_u(TA)$ modes (taking z as the direction of propagation). The remaining six optical branches are identified as A_{1g}, E_g (even-parity) and A_{2u}, E_u (odd-parity) modes. The even-parity modes will be Raman active, while the odd-parity optical modes will be infrared active.

With the use of symmetry, the following relations among force-constant matrices are found. For the nearest-neighbor Pb-I interactions, we have

$$\Phi(1,2)=\begin{pmatrix}A_1&0&D_1\\0&B_1&0\\E_1&0&C_1\end{pmatrix}=C_3\Phi(1,2')C_3^{-1}$$
$$=C_3^{-1}\Phi(1,2'')C_3.$$

For the nearest-neighbor I-I interactions, we have

$$\Phi(2,3)=\begin{pmatrix}A_2&D_2&E_2\\D_2&B_2&F_2\\E_2&F_2&C_2\end{pmatrix}=C_3\Phi(2,3')C_3^{-1}$$
$$=C_3^{-1}\Phi(2,3'')C_3.$$

For the next nearest-neighbor I-I interactions, we have

$$\Phi(2,\overline{3})=\begin{pmatrix}A_3&D_3&E_3\\D_3&B_3&F_3\\E_3&F_3&C_3\end{pmatrix}=C_3\Phi(2,\bar{3}')C_3^{-1}$$
$$=C_3^{-1}\Phi(2,\bar{3}')C_3.$$

Here $\bar{3}$ denotes an I atom 3 displaced by a lattice vector $-(0,0,1)c$ (see Fig. 1). All the other short-range couplings are ignored, as they are found to have less influence on the phonon-dispersion curves.

The long-range Coulomb interaction matrix is calculated via the Ewald method by assuming a point charge $+e$ at the Pb sites and $-e/2$ at the I sites. To take into account the anisotropy, the 3×3 Coulomb matrix between any two ions is multiplied by the effective charge matrix given by

$$\begin{pmatrix}e_T^*&0&0\\0&e_T^*&0\\0&0&e_L^*\end{pmatrix},$$

where e_T^* and e_L^* are the transverse and longitudinal effective dynamic charges for the Pb atom, which are treated as adjustable parameters to fit the LO-TO splittings of the E_u and A_{2u} optical modes. Including the 17 parameters for short-range force constants, we have a total of 19 adjustable parameters which are used in the fit of phonon-dispersion curves.

We fit the lowest four phonon branches to the neutron-scattering data of Ref. 10 and the zone-center phonon frequencies for the E_u(TO), E_u(LO), B_g, A_{1u}(TO), and A_{2u}(LO) modes obtained from the far-infrared reflectance[11,12] and Raman-scattering data.[13] The best-fit pa-

TABLE II. Parameters used in the rigid-ion model (measured in units of e^2/v_c, where v_c is the unit-cell volume). e_l^* and e_t^* are dimensionless.

A_1	B_1	C_1	D_1	E_1	e_l^*	e_t^*
-9.18828	2.93684	-6.38286	3.82050	-10.09855	3.59933	2.57632
A_2	B_2	C_2	D_2	E_2	F_2	
-3.30617	2.71029	-6.01193	0.94633	3.60113	-2.87162	
A_3	B_3	C_3	D_3	E_3	F_3	
-1.35993	-4.65746	3.27137	-0.94474	-1.86858	4.62527	

rameters are given in Table II. The theoretical predictions for the phonon-dispersion curves are shown in Fig. 2. The fit of the lowest four branches to the neutron-scattering data is very good. The comparison of theory and experiment for the zone-center phonon frequencies is given in Table III and that for the sound velocities is given in Table IV. As seen in these tables, the agreement between theory and experiment is quite good.

Since PbI_2 is anisotropic, we expect that the long-wavelength optical-phonon modes to display an angular dispersion. This is shown in Fig. 3, in which the phonon frequencies as functions of the angle θ (where $\cos\theta = q_x/q_z$) as the phonon wave vector approaches zero are plotted. It is noted that only the E_u and A_{2u} modes which are infrared active have angular dispersion. The angular dispersion for the E_u mode is quite large, and it tends to cross the dispersion curve of the A_{2u} mode. The two modes ''anticross'' at $\theta \approx 0.8(\pi/2)$ as a result of level repulsion. Thus, there is a switch of characters at $\theta = \pi/2$ such that the E_u(LO) mode lies higher than the A_{2u}(TO) mode. As we shall see in the next two sections, this angular dependence plays a significant role in determining the anisotropy of the carrier mobilities.

III. POLAR-OPTICAL SCATTERING

In the E_u and A_{2u} optical modes, ions with opposite charges vibrate against each other, thus giving rise to a long-range macroscopic electric field. The interaction of a carrier with such[9] a field is known as polar-optical scattering (or Frölich scattering).[17] Due to the strong polarity of the material, it is expected that the polar-optical scattering will be the dominant mechanism which determines the intrinsic carrier mobility at temperatures above about 77 K. This has been confirmed theoretically for HgI_2,[16] a system of similar polarity. The electron-phonon interaction due to polar-optical scattering associated with mode j is given by

$$H_{\text{el-ph}} = \frac{1}{\sqrt{N M_{\text{cell}}}} \sum_{\mathbf{q},\alpha} \sqrt{\frac{M_{\text{cell}}}{M_\alpha}} \frac{e}{v_c} \left[\frac{e^*_{\alpha,l} \hat{\epsilon}^{(j)}_{\alpha,l}}{\epsilon_l(\infty)} + \frac{e^*_{\alpha,t} \hat{\epsilon}^{(j)}_{\alpha,t}}{\epsilon_t(\infty)} \right] \cdot \hat{q} \left(\frac{4\pi}{q} \right) Q_{\mathbf{q}j} e^{i\mathbf{q}\cdot\mathbf{r}}, \quad (1)$$

where e is the free-electron charge, $e^*_{\alpha,l}(e^*_{\alpha,t})$ is the longitudinal(transverse) effective dynamic charge of ion α, $\epsilon_l(\infty)[\epsilon_t(\infty)]$ is the longitudinal [transverse] high-frequency dielectric constant, $\hat{\epsilon}^{(j)}_\alpha$ is the polarization vector, and v_c is volume of the unit cell. e_t^* has been determined by reflectivity measurements to be $2.8e$ for the Pb ion,[11] while our theoretical value (obtained by fitting the LO-TO splitting of the E_u mode) is $3.60e$ (see Table II). e_l^* has not been determined experimentally as it is difficult to obtain PbI_2 crystals suitable for performing reflectivity measurements with the electric field of the incident photon parallel to the c axis. The theoretical value obtained is $e_l^* = 2.58$ which gives a resonable LO-TO splitting of the A_{2u} mode inferred from the dielectric measurement.[18]

The effect of polar-optical scattering can be described by an angular-dependent coupling constant defined as

$$C_j(\mathbf{q}) = 4\pi \left| \sum_\alpha \sqrt{\frac{M_{\text{cell}}}{M_\alpha}} \frac{e}{v_c} \left[\frac{e^*_{\alpha,l} \hat{\epsilon}^{(j)}_{\alpha,l}}{\epsilon_l(\infty)} + \frac{e^*_{\alpha,t} \hat{\epsilon}^{(j)}_{\alpha,t}}{\epsilon_t(\infty)} \right] \cdot \hat{q} \right|. \quad (2)$$

Note that $C_j(\theta)/q$ plays the same role as a deformation potential constant in the deformation-potential scattering.

Using the displacement vectors obtained by the rigid-ion model, we can obtain the angular-dependent coefficients $C_j(\theta_q)$ for the E_u and A_{2u} optical modes. In Fig. 4, we plot the angular-dependent coupling coefficient C_j for the two

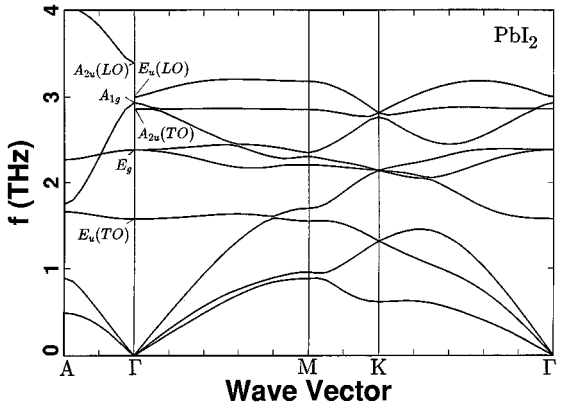

FIG. 2. Phonon-dispersion curves of PbI_2 obtained by the present rigid-ion model. The symmetries of zone-center optical modes are marked.

TABLE III. Zone-center phonon frequencies (in THz) for PbI_2 obtained in the present rigid-ion model and from various experimental measurements.

	E_u(TO)	E_u(LO)	E_g	A_{1g}	A_{2u}(TO)	A_{2u}(LO)
Theory	1.578	3.004	2.382	2.934	2.861	3.396
Experiment	1.55 [a]	3.18 [b]	2.34 [b]	2.94 [b]	2.85 [b]	3.39 [b]

[a] Lucovsky *et al.* (Ref. 11).

[b] Grisel and Schmid (Ref. 13).

TABLE IV. Sound velocities (in 10^5 cm/s) of acoustical branches for PbI_2 obtained in the present rigid-ion model. The values in parentheses are experimental data taken from Ref. 10.

$[00\xi]$	$[\xi\xi 0]$	$[\xi 00]$
v_l= 1.392(1.54)	v_l=1.892 (1.81)	v_l= 1.944 (1.86)
v_t= 1.073(0.93)	$v_{t,\parallel}$=1.438 (1.10)	$v_{t,\parallel}$= 1.225 (1.07)
	$v_{t,\perp}$=0.777 (0.86)	$v_{t,\perp}$=0.990 (0.94)

infrared-active optical branches (E_u and A_{2u}). The two modes are found to couple strongly at finite values of θ, resulting in an unusual angular dependence of C_j. In the uncoupled case (such as in HgI_2), $C_j(\theta)$ for the E_u (A_{2u}) mode should approximately behave like the function $\sin^2\theta$ ($\cos^2\theta$). However, with the strong coupling in the present case, the angular dependence is completely changed. At finite θ, we can no longer assign the lower (upper) branch to the E_u (A_{2u}) mode. Thus, from now on, we shall simply call them the lower and upper branches.

The scattering rate from state $\mathbf{k}$ to $\mathbf{k}'$ due to polar-optical scattering associated with branch j is given by

$$W_j(\mathbf{k},\mathbf{k}')=\frac{1}{8\pi^2\rho}\int\frac{C_j^2(\theta_q)}{\omega_j(\theta_q)q^2}\{n(\omega_j(\theta_q))\delta_{\mathbf{k}',\mathbf{k}+\mathbf{q}}\delta(E_{\mathbf{k}'}-E_{\mathbf{k}}-\hbar\omega_j(\theta_q))+[n(\omega_j)+1]\delta_{\mathbf{k}',\mathbf{k}-\mathbf{q}}\delta(E_{\mathbf{k}'}-E_{\mathbf{k}}+\hbar\omega_j)\}d\mathbf{q}. \tag{3}$$

For $\mathbf{k}(\mathbf{k}')$ along a general direction, the inclusion of both the anisotropy of band structure and the phonon dispersion is complicated. We therefore approximate $\omega_j(\theta_q)$ by a constant $\overline{\omega_j}$, which is taken to be the value of ω at the angle θ_q where the coupling strength C_j is the maximum. From Fig. 4, we see that the maximum occurs at $\theta_q=0.75(\pi/2)$ for the lower branch and at $\pi/2$ for the upper branch. Thus, we have $\overline{\omega_1}$=2.60 THz and $\overline{\omega_2}$=3.396 THz (see Fig. 3).

We define new variables

$$q_i^*=\sqrt{\sigma}q_i \quad \text{for} \quad i=x,y$$

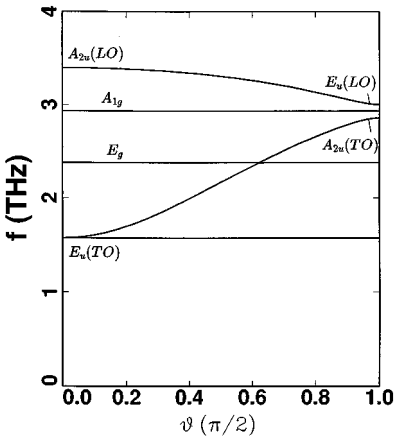

FIG. 3. Angular dispersion of phonon frequencies for PbI_2 deduced from the present rigid-ion model.

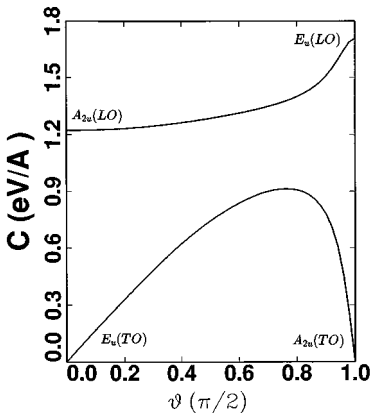

FIG. 4. Angular dependence of the coupling coefficient for polar-optical phonon scattering for the two infrared active modes.

and $q_z^*=q_z$, where $\sigma\equiv m_l^*/m_t^*$ and similarly for $\mathbf{k}^*(\mathbf{k}'^*)$, so that $E_{\mathbf{k}}(E_{\mathbf{k}'})$ becomes a spherical function of $\mathbf{k}^*(\mathbf{k}'^*)$. Equation (3) becomes

$$W_j(\mathbf{k},\mathbf{k}')=\frac{\overline{C_j^2}}{8\pi^2\rho\overline{\omega_j}}\int\frac{d\mathbf{q}^*}{q^{*2}}\{n(\overline{\omega_j})\times\delta_{\mathbf{k}^{*\prime},\mathbf{k}^*+\mathbf{q}^*}\delta(E_{\mathbf{k}'}-E_{\mathbf{k}}-\hbar\overline{\omega_j})+[n(\overline{\omega_j})+1]\delta_{\mathbf{k}^{*\prime},\mathbf{k}^*-\mathbf{q}^*}\delta(E_{\mathbf{k}'}-E_{\mathbf{k}}+\hbar\overline{\omega_j})\}, \tag{4}$$

where $\overline{C_j^2}$ is defined by

$$\overline{C_j^2}=\int_{-1}^{1}\frac{C_j^2(\theta_q)}{\sin^2\theta_q^*+\sigma\cos^2\theta_q^*}d\cos\theta_q^*/2. \tag{5}$$

The values of $\overline{C_j}$ are listed in Table V.

IV. CARRIER MOBILITY

To calculate the carrier mobility, we also need the momentum relaxation time τ_i (the subscript i denotes the direction of transport) which is related to the scattering rate via the expression[19]

$$\frac{1}{\tau_i(E)}=\int k_i(k_i-k_i')W(\mathbf{k}',\mathbf{k})d\mathbf{k}'\times\delta(E-E_{\mathbf{k}})d\mathbf{k}\Big/\int k_i^2\delta(E-E_{\mathbf{k}})d\mathbf{k}, \tag{6}$$

where $W(\mathbf{k}',\mathbf{k})$ is the scattering rate given in the previous section. Substituting Eq. (5) into Eq. (6) we obtain

TABLE V. Spherical average of the coupling coefficients for polar-optical scatterings ($\overline{C_j}$) associated with E_u and A_{2u} modes for three different longitudinal to transverse effective mass ratios (σ). The units are eV/Å^2.

	$\sigma=1$	$\sigma=2$	$\sigma=5$
E_u	0.737	0.671	0.574
A_2	1.378	1.275	1.134

$$\frac{1}{\tau_l(E)}=\frac{3\hbar^3}{16\pi^2\rho(2m_l^*E)^{3/2}}\times\sum_j\int_{-k_m}^{k_m}dk_zk_z\int d\phi_q^*\int_0^\pi d\theta_q^*\times\frac{C_j^2(\theta_q)\cos\theta_q^*\sin\theta_q^*}{\omega_j(\sin^2\theta_q^*+\sigma\cos^2\theta_q^*)}\{-n(\omega_j)[q_+^{(1)}/R_+(q_+^{(1)})+q_+^{(2)}/R_+(q_+^{(2)})]+[n(\omega_j)+1][q_-^{(1)}/R_-(q_-^{(1)})+q_-^{(2)}/R_-(q_-^{(2)})]\},\tag{7}$$

$$\frac{1}{\tau_t(E)}=\frac{3\hbar^3}{32\pi^2\rho(2m_l^*E)^{3/2}}\sum_j\int_{-k_m}^{k_m}(k_m^2-k_z^2)^{1/2}dk_z\times\int d\phi_q^*\int_0^\pi d\theta_q^*\frac{C_j^2(\theta_q)\sin^2\theta_q^*\cos\phi_q^*}{\omega_j(\sin^2\theta_q^*+\sigma\cos^2\theta_q^*)}\times\{-n(\omega_j)[q_+^{(1)}/R_+(q_+^{(1)})+q_+^{(2)}/R_+(q_+^{(2)})]+[n(\omega_j)+1][q_-^{(1)}/R_-(q_-^{(1)})+q_-^{(2)}/R_-(q_-^{(2)})]\},\tag{8}$$

where $k_m=\sqrt{2m_l^*E}/\hbar$, $R_\pm(q)=(\hbar^2/m_l^*)|q\pm(k_z\cos\theta_q^*+(k_m^2-k_z^2)^{1/2}\sin\theta_q^*\cos\phi_q^*)|$. $q_\pm^{(1)}$ and $q_\pm^{(2)}$ are two positive real roots of the equation

$$\frac{\hbar^2}{2m_l^*}[q^2\pm2q(k_z\cos\theta_q^*+(k_m^2-k_z^2)^{1/2}\sin\theta_q^*\cos\phi_q^*)]=\pm\hbar\omega_j.$$

Here θ_q^* is the polar angle of $\mathbf{q}^*$ with respect to the c axis and ϕ_q^* is the azimuthal angle between $\mathbf{q}^*$ and $\mathbf{k}$.

If we replace $C_j^2(\theta_q)/(\sin^2\theta_q^*+\sigma\cos^2\theta_q^*)$ by its spherically averaged values, C_j and $\omega_j(\theta_q)$ by $\overline{\omega_j}$ [values evaluated at maximum $C_j(\theta_q)$], the above results reduce to[19]

$$\frac{1}{\tau(E)}=\frac{\overline{C_j^2}}{4\pi\rho\hbar\overline{\omega_j}v_E}n(\overline{\omega_j})\left[\sqrt{1+\frac{\hbar\overline{\omega_j}}{E}}-\frac{\hbar\overline{\omega_j}}{E}\sinh^{-1}\sqrt{\frac{E}{\hbar\overline{\omega_j}}}\right]+[n(\overline{\omega_j})+1]\left[\sqrt{1-\frac{\hbar\overline{\omega_j}}{E}}+\frac{\hbar\overline{\omega_j}}{E}\sinh^{-1}\sqrt{\frac{E}{\hbar\overline{\omega_j}}-1}\right],\tag{9}$$

where $v_E=\sqrt{2E/m_l^*}$.

Momentum relaxation rates ($1/\tau_l$ and $1/\tau_t$) at 300 K due to polar-optical scattering are plotted in Fig. 5 for three different mass anisotropies $m_l^*/m_t^*\equiv\sigma=1,2$, and 5 with m_l^* assumed equal to the free-electron mass, m_0. The solid (dashed) curves are for $1/\tau_l$ ($1/\tau_t$) and the dotted curves are the polar-optical scattering rates ($1/\tau$) calculated in the spherical model according to Eq. (9). For carriers with a longitudinal effective mass differing from m_0, the result simply scales according to $\sqrt{m_l^*/m_0}$ [see Eq. (9)]. In Fig. 5, the two shoulder structures are due to the onset of the optical-phonon emission for the two branches with the higher branch being stronger. It is noted that even for spherical band ($\sigma=1$) $1/\tau_l$ and $1/\tau_t$ are different by about 30% due to the anisotropy in the scattering rate.

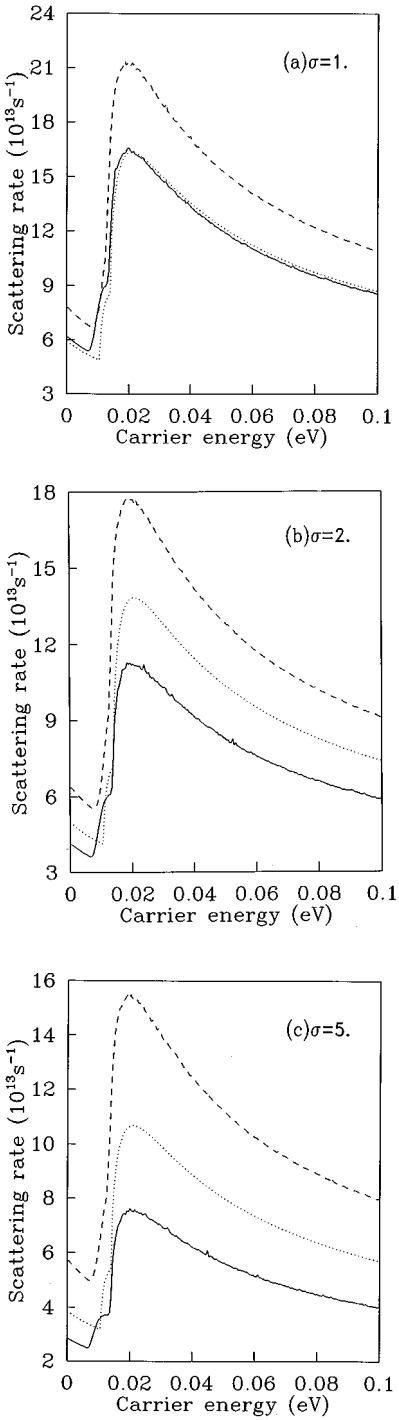

FIG. 5. Momentum relaxation rates associated with polar-optical scattering at 300 K as functions of the carrier energy for three values of mass anisotropies: (a) $\sigma=1$, (b) $\sigma=2$, (c) $\sigma=5$. Solid curves: τ_l^{-1}. Dashed curves: τ_t^{-1}. Dotted curve: τ^{-1} (spherical model).

Finally the mobilities are related to the momentum relaxation times via[19]

$$\mu_l=\frac{e}{m_l^*}\frac{\langle E\tau_l(E)\rangle}{\langle E\rangle},$$

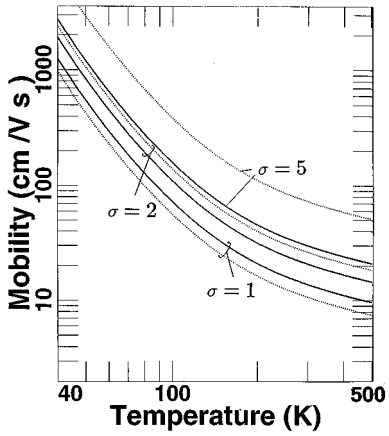

FIG. 6. Carrier mobilities as functions of temperature for three values of mass anisotropies, $\sigma = 1,2$, and 5. Solid (dotted) curves are for transport parallel (perpendicular) to the c axis.

$$\mu_t = \frac{e}{m_t^*} \frac{\langle E\tau_t(E)\rangle}{\langle E\rangle},$$

where $\langle\ \rangle$ denotes a thermal average with a Boltzmann distribution in the nondegenerate limit. To simplify the calculation, we use the spherical-model expression [Eq. (9)] for the polar-optical scattering, but scale it by appropriate factors to take into account the anisotropy of scattering rates. As shown in Fig. 5, τ_l^{-1} and τ_t^{-1} differ from the spherical results $(1/\tau)$ approximately by an energy-independent factor. We find $\tau_l^{-1} \approx f_l \tau^{-1}$ and $\tau_t^{-1} \approx f_t \tau^{-1}$ with $f_l = 1.0,\ 0.812,\ 0.701$ and $f_t = 1.287,\ 1.283,\ 1.439$ for $\sigma = 1,\ 2,\ 5$.

Figure 6 shows the mobility as a function of temperature for a carrier with $m_l^* = m_0$ and with three different values of m_t^*/m_l^* Note that the carrier mobility scales like $m_l^{*-3/2}$ (since τ scales like $m_l^{*-1/2}$). The existing estimates of the effective masses of PbI_2 are quite uncertain. The cyclotron measurement[14] gives an electron polaron mass $(m_l^* m_t^*)^{1/2} = 0.68 \pm 0.16 m_0$. Based on the band-structure calculation,[9] m_l^* is greater than m_t^* but the ratio is not known accurately. Assuming $\sigma = 2$, we obtain $m_l^* \approx 0.96 m_0$ and the electron mobilities $\mu_l(\mu_t) \approx 110(140)$ $cm^2/V\,s$ and $20(25)$ $cm^2/V\,s$ at 100 and 300 K, respectively. The results are in agreement with the experimental data within a factor of 3.[14,15] The temperature dependence of the mobility goes approximately like $1/T^{1.3}$ for temperatures between 40 and 100 K, which agrees fairly well with the measurements of Ref. 14. For holes, the calculated hole effective masses are $m_l^* \approx 1.67 m_0$ and $m_t^* \approx 0.35 m_0$ which gives $m_l^*/m_t^* \approx 5$.[20] Using these values, we obtain the room-temperature hole mobilities $\mu_t \approx 34$ $cm^2/V\,s$ and $\mu_l \approx 15$ $cm^2/V\,s$. These numbers are about one order of magnitude higher than the observed hole mobilities,[15] indicating that the extrinsic scattering mechanism may be important here.

Although there are uncertainties with the effective dynamic charges and the effective masses used in the calculation, the overall estimate should be correct within a factor of 3. The fairly good agreement for the electron mobilities between theory and experiment at room temperature (within a factor of 3) indicates that the intrinsic mechanism due to polar-optical scattering is probably the dominant factor in explaining the observed electron mobility, while the hole mobility may be more influenced by the extrinsic scattering mechanisms.

V. CONCLUSION

We have presented detailed theoretical studies of the phonon-dispersion curves, electron-phonon interaction due to polar-optical scattering, and carrier mobilities of $2H$ PbI_2. The phonon-dispersion curves obtained in the rigid-ion model with 19 empirical parameters agree well with the neutron-scattering data for the lowest four branches and with the far-infrared as well as Raman-scattering data for all zone-center optical modes. The amount of angular dispersion for the two infrared-active optical modes (E_u and A_{2u}) is also in agreement with the reflectivity measurements. The effective dynamic charges which are adjusted to give rise to the correct angular dispersion for the E_u and A_{2u} optical modes are used in the calculation of the polar-optical scattering. The carrier mobilities due to the polar-optical scattering are then calculated. Both the magnitudes and anisotropy of carrier mobilities and their temperature dependence from 40 to 100 K are found in qualitative agreement with experiment.

ACKNOWLEDGMENT

This work is supported in part by the Department of Energy.

[1] See, for example, J. C. Lund, F. Olschner, and A. Burger, in *Semiconductors and Semimetals*, edited by T. E. Schlesinger and R. B. James (Academic, New York, 1995), Chap. 11, and references therein.

[2] G. Margaritondo, J. E. Rowe, M. Schlüter, and G. K. Wertheim, Phys. Rev. B **16**, 2934 (1977).

[3] I. Imai, J. Phys. Chem. Solids **22**, 81 (1961).

[4] G. Baldini and S. Franchi, Phys. Rev. Lett. **26**, 503 (1971).

[5] G. Harbeke and E. Tosatti, Phys. Rev. Lett. **28**, 1567 (1972).

[6] I. Baltog, I. Piticu, M. Constantinescu, C. Ghita, and L. Ghita, Phys. Status Solidi A **52**, 103 (1979).

[7] E. Doni, G. Grosso, and G. Spavieri, Solid State Commun. **11**, 493 (1972).

[8] L. Ch. Schlüter and M. Schlüter, Phys. Status Solidi B **57**, 145 (1973).

[9] L. Ch. Schlüter and M. Schlüter, Phys. Rev. B **9**, 1652 (1974).

[10] B. Dorner, R. E. Ghosh, and G. Harbeke, Phys. Status Solidi B **73**, 655 (1976).

[11] G. Lucovsky, R. M. White, W. Y. Liang, R. Zallen, and Ph. Scmid, Solid State Commun. **18**, 811 (1978).

[12] J. Hiraishi, K. Tani, and T. Tamura, J. Chem. Phys. **71**, 554 (1979).

[13] A. Grisel and Ph. Schmid, Phys. Status Solidi B **73**, 587 (1976).
[14] P. D. Bloch, J. W. Hodby, T. E. Jenkins, D. W. Stacey, G. Lang, F. Levy, and C. Schwab, J. Phys. C **11**, 4997 (1978).
[15] R. Minder, G. Ottaviani, and C. Canali, J. Phys. Chem. Solids **37**, 417 (1976).
[16] Y. C. Chang and R. B. James, Phys. Rev. B **53**, 14 200 (1996).
[17] H. Frölich, Proc. R. Soc. London Ser. A **160**, 230 (1937).
[18] A. E. Dugan and H. K. Henisch, J. Phys. Chem. Solids **35**, 1269 (1974).
[19] B. K. Ridley, *Quantum Process in Semiconductors* (Oxford, New York, 1982).
[20] G. Grosso (unpublished) (quoted in Ref. 14).